Biosensors and Bioelectronics xxx (xxxx) xxx

Contents lists available at ScienceDirect

Biosensors and Bioelectronics

journal homepage: http://www.elsevier.com/locate/bios

Real-time nanoplasmonic sensing of three-dimensional morphological changes in a supported lipid bilayer and antimicrobial testing applications

Bo Kyeong Yoon [a], Hyeonjin Park [a,b], Vladimir P. Zhdanov [c], Joshua A. Jackman [a,**], Nam-Joon Cho [b,*]

[a] School of Chemical Engineering and Biomedical Institute for Convergence at SKKU (BICS), Sungkyunkwan University, Suwon, 16419, Republic of Korea
[b] School of Materials Science and Engineering, Nanyang Technological University, 50 Nanyang Avenue 639798, Singapore
[c] Boreskov Institute of Catalysis, Russian Academy of Sciences, Novosibirsk, 630090, Russia

ARTICLE INFO

Keywords:
Nanoplasmonics
Localized surface plasmon resonance
Label-free biosensing
Artificial cell membrane
Antimicrobial

ABSTRACT

We report the development of a real-time localized surface plasmon resonance (LSPR) biosensing strategy to detect three-dimensional morphological changes in a supported lipid bilayer (SLB) on a plasmonic substrate. The sensing concept advances on past efforts to detect subtle conformational changes in adsorbed biomacromolecules by demonstrating the capability to track large-scale, complex adsorbate shape changes and to classify different types of shape changes based on specific, multi-step measurement signatures. To validate this concept, we tested the addition of antimicrobial fatty acids, monoglycerides, and surfactants in micellar form to the SLB platform, which triggered specific three-dimensional membrane morphological changes such as tubule or bud formation along with solubilization. Experimentally, the different remodeling events were detected by distinct measurement signatures related to the shape and size of lipid protrusions that formed and evolved over time, which agreed well with a newly developed theoretical model. Our conceptual approach and formalism are applicable to various biosensing techniques, including not only LSPR but also surface plasmon resonance (SPR) and total internal reflection fluorescence (TIRF) microscopy. These sensing capabilities are advantageous for evaluating the mechanisms of antimicrobial drug candidates and other membrane-active compounds, and the measurement strategy is extendable to a wide range of biomimetic lipid compositions.

1. Introduction

There is broad interest in developing real-time biosensing strategies to characterize cell-membrane-mimicking supported lipid bilayer (SLB) interactions with a wide range of biomacromolecules and biological nanoparticles, such as peptides, proteins, micelles, exosomes, and virus particles, as well as with drug delivery vehicles, *e.g.*, liposomes and lipid nanoparticles (Buck et al., 2019; Han et al., 2019; Nishio et al., 2020; Park et al., 2019). One of the most challenging measurement aspects is to track SLB morphological changes, which result from biomacromolecular interactions and are relevant to various biological phenomena and pharmaceutical drug testing applications. Key examples include cholesterol-induced membrane remodeling and three-dimensional crystallization (Lee et al., 2020; Rahimi et al., 2016; Varsano et al., 2015), and antiviral drug development to inhibit membrane-associated viral genome replication (Cho et al., 2010, 2016). Currently used biosensing techniques include surface plasmon resonance (SPR) (Ryu et al., 2019; Soler et al., 2018), total internal reflection fluorescence (TIRF) microscopy (Mapar et al., 2018), evanescent light scattering (Agnarsson et al., 2016), and quartz crystal microbalance with dissipation (QCM-D) (Di Iorio et al., 2020), which all have penetration depths of about 100–250 nm while the SLB thickness is much shorter (~5 nm). On the other hand, nanoplasmonic sensors can exhibit penetration depths of ~20 nm or less that are more comparable to the SLB thickness and thus potentially more sensitive to membrane morphological changes (Bruzas et al., 2016; Jose et al., 2013; Oh and Altug, 2018).

While nanoplasmonic sensing experiments are typically conducted on metal nanoparticle surfaces, indirect nanoplasmonic sensing (INPS) platforms enable the use of silica-coated gold nanodisk arrays on which SLBs can readily form (Langhammer et al., 2010). The embedded nanodisks exhibit localized surface plasmon resonance (LSPR), whereby

* Corresponding author.
** Corresponding author.
E-mail addresses: jjackman@skku.edu (J.A. Jackman), njcho@ntu.edu.sg (N.-J. Cho).

https://doi.org/10.1016/j.bios.2020.112768
Received 6 August 2020; Received in revised form 3 October 2020; Accepted 23 October 2020
Available online 31 October 2020

light extinction induces the collective oscillation of conduction-band electrons within the nanodisk that gives rise to an enhanced electromagnetic field in close proximity to the silica coating, which is the active sensing interface (Dahlin et al., 2013; Jackman et al., 2017a; Unser et al., 2015). This field is scattered by adsorbate molecules that induce changes in collective electromagnetic oscillations. Physically, this sensing concept is similar to SPR and the main difference is in the type of evanescent field that is generated by the sensor (exponential in the SPR case vs. dipole-like in the LSPR case) and the degree of surface sensitivity. Experimentally, the LSPR sensing approach has been widely utilized to detect subtle conformational changes involving adsorbed liposomes, SLBs, and proteins that can be modeled as a uniform film or spherically shaped objects (Ferhan et al., 2018; Jackman et al., 2017b, 2017c). However, various types of biologically relevant biomacromolecular interactions involve more complex, non-uniform adsorbate shape changes and there is an outstanding need to develop advanced nanoplasmonic sensing approaches to track such changes.

Herein, using a combination of experimental and theoretical approaches, we developed a real-time LSPR biosensing strategy to detect and classify complex adsorbate shape changes based on proof-of-concept experiments involving three-dimensional membrane morphological changes in an SLB platform. Specifically, we evaluated the LSPR measurement responses that occur when membrane-active, antimicrobial compounds interact with an SLB platform on a silica-coated gold nanodisk array and give rise to complex, dynamic changes in three-dimensional membrane morphology. The test compounds included two of the most biologically active fatty acids and monoglycerides termed lauric acid (LA) and glycerol monolaurate (GML), respectively, along with a related surfactant, sodium dodecyl sulfate (SDS), all of which demonstrate potent antimicrobial effects by disrupting the lipid membranes surrounding bacteria and enveloped viruses (Yoon et al., 2018). The mechanistic details of how each compound disrupts phospholipid membranes remain under investigation and we demonstrate how the LSPR technique is well-suited to address this measurement need as well as its compelling advantages compared to other biosensing techniques used in past works. Furthermore, the sensing concepts developed in our work and the underlying theoretical formalism are broadly useful for not only LSPR measurements but also readily extendable to the SPR and TIRF microscopy techniques as well.

2. Materials and methods

2.1. Reagents

Stock solutions of 1,2-dioleoyl-*sn*-glycero-3-phosphocholine (DOPC) and 1,2-dihexanoyl-*sn*-glycero-3-phosphocholine (DHPC) lipids in chloroform were obtained from Avanti Polar Lipids (Alabaster, AL). SDS and LA in lyophilized form were obtained from Sigma-Aldrich (St. Louis, MO). GML in lyophilized form was obtained from Abcam (Cambridge, UK). An aqueous buffer solution consisting of 10 mM Tris [pH 7.5] with 150 mM NaCl was used and prepared with deionized water (>18 MΩ cm).

2.2. SLB fabrication

DOPC SLBs were fabricated on silica-coated LSPR sensor chips by depositing DOPC/DHPC lipid bicelles onto the sensor surface, as previously described (Kolahdouzan et al., 2017). The molar ratio of DOPC to DHPC phospholipids in the bicelles was 0.25 and the bicelles were prepared at a total lipid concentration of 5 mM. The bicelle sample was diluted 32-times before experiment.

2.3. LSPR measurements

The experiments were conducted on silica-coated gold nanodisk arrays by using an Insplorion XNano instrument (Insplorion AB, Gothenburg, Sweden), as previously described (Jackman et al., 2014). Before experiment, the sensor chip was rinsed with water and ethanol, and then treated with oxygen plasma by using a CUTE-1MPR machine (Femto Science Inc., Hwaseong, Republic of Korea). Afterwards, the sensor chip was placed within the measurement chamber and liquid samples were injected under continuous flow conditions by using a peristaltic pump (Reglo Digital MS-4/6, Ismatec, Glattsburg, Switzerland) at a volumetric flow rate of 100 μL/min. The optical extinction spectrum was measured in transmission mode and the centroid position was determined (Dahlin et al., 2006). The extinction spectrum was recorded every 1 s and data analysis was performed using the Insplorer software package (Insplorion AB).

3. Results and discussion

3.1. LSPR sensing experiments

We conducted LSPR experiments using a silica-coated gold nanodisk array upon which a fluid-phase DOPC SLB coating was fabricated and served as the biosensing interface (Fig. 1a). The gold nanodisk transducers had diameter and height of around 100 and 20 nm, respectively. Transmission-mode optical extinction measurements showed that the silica-coated gold nanodisk array on a glass substrate, which was housed within a microfluidic chamber, had an ensemble-average, maximum-intensity LSPR wavelength (λ_{max}) position around 715 nm in aqueous buffer solution (Fig. 1b). Real-time interaction processes were tracked by monitoring the $\Delta\lambda_{max}$ shift, which reflects changes in the local refractive index near the sensor surface (Špačková et al., 2016). A DOPC SLB on the sensor surface was fabricated by the bicelle method (Jackman and Cho, 2020). Two-stage SLB formation kinetics were observed due to bicelle adsorption and fusion, and the rate of increase in the $\Delta\lambda_{max}$ signal was greater in the second stage of the formation process, which is related to reorganization of adsorbed lipid molecules to form the SLB (Sut et al., 2019) (Fig. 1c). More specifically, during the first stage, bicelles adsorb in the diffusion-limited fashion and remain intact on the sensor surface. After a critical surface coverage of adsorbed bicelles is reached, there is a transition to the second stage and the greater rate of increase in the $\Delta\lambda_{max}$ signal during the latter stage occurs due to diffusion-limited adsorption of newly arriving bicelles along with fusion and rupture of already adsorbed bicelles to form an SLB, whereby adsorbed phospholipid molecules move, on average, closer to the sensor surface. The final $\Delta\lambda_{max}$ shift due to SLB formation was around 2.98 ± 0.11 nm, which agrees with literature values (Jackman et al., 2016; Sut et al., 2019).

After SLB formation, we then added SDS, LA, or GML to the DOPC SLB platform under continuous flow conditions and tracked the real-time interaction kinetics. We tested SDS, LA, and GML micelles because all three compounds exhibit membrane-disruptive activity mainly in the micellar state. The tested concentrations of 2 mM SDS, 2 mM LA, and 500 μM GML were selected because the corresponding critical micelle-formation concentration values in equivalent solution conditions are around 800 μM, 900 μM, and 60 μM, respectively (Yoon et al., 2017, 2020). Fig. 2 presents the time-resolved LSPR measurement responses corresponding to the interactions of SDS, LA, and GML with DOPC SLBs. We discuss each case for SDS, LA, and GML individually below.

The addition of 2 mM SDS to a DOPC SLB caused a rapid drop in the $\Delta\lambda_{max}$ signal within 2 min (Fig. 2a). The corresponding $\Delta\lambda_{max}$ shift was around −3 nm, which indicates that the DOPC SLB adlayer was removed from the sensor surface (Yoon et al., 2015). A subsequent buffer washing step caused no further change in the $\Delta\lambda_{max}$ signal. Closer inspection of the measurement kinetics showed that the initial rate of decrease in the $\Delta\lambda_{max}$ signal was sharp, with around 60% of the $\Delta\lambda_{max}$ shift occurring in the first 30 s of the SDS-DOPC SLB interaction process and likely related to transient tubule formation (Yoon et al., 2015). Thereafter, the rate of decrease in the $\Delta\lambda_{max}$ signal was more moderate and exhibited minor

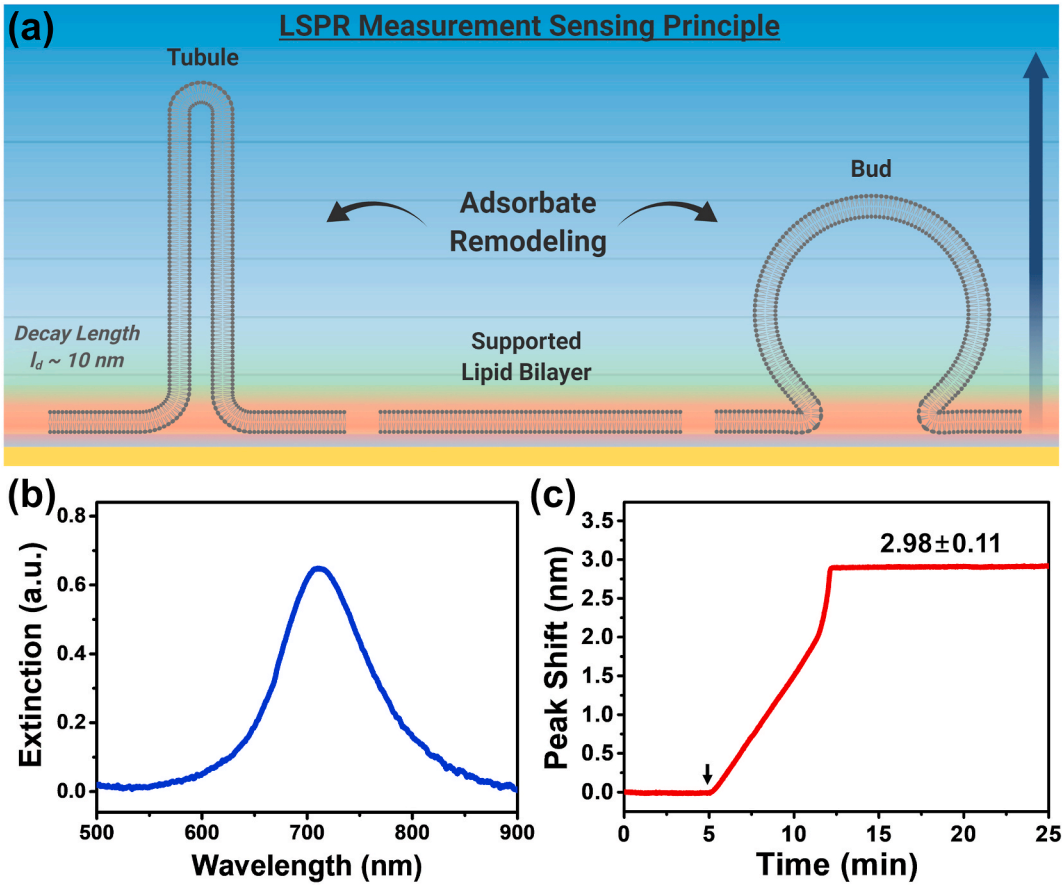

Fig. 1. Overview of nanoplasmonic sensing strategy. (a) Schematic illustration of LSPR sensing concept to track three-dimensional membrane morphological changes. (b) Representative optical extinction spectrum for a silica-coated gold nanodisk array in aqueous buffer solution. (c) Real-time $\Delta\lambda_{max}$ measurement tracking SLB formation kinetics on a silica-coated gold nanodisk array. An initial baseline in aqueous buffer solution was recorded before bicelles were added under continuous flow conditions starting at $t = 5$ min (see arrow). Kinetic data are shown from a single, representative experiment. The mean ± standard deviation of the $\Delta\lambda_{max}$ shift corresponding to SLB formation (relative to measurement baseline) is listed and reported based on 9 independent experiments.

fluctuations in the slope, which are likely related to structural changes that occurred during membrane solubilization.

The addition of 2 mM LA to a DOPC SLB also caused a rapid drop in the $\Delta\lambda_{max}$ signal, however, the $\Delta\lambda_{max}$ shift in this case was appreciably smaller with a value around −0.4 nm (Fig. 2b). This result supports that the DOPC SLB adlayer remains mainly intact while the negative $\Delta\lambda_{max}$ shift indicates either a net loss of adsorbed mass due to LA-induced membrane lysis and/or membrane remodeling events that cause the spatial proximity of adsorbed lipid molecules to move away, on average, from the sensor surface. The relatively small magnitude of the measurement response is consistent with out-of-plane tubule formations in the DOPC SLB (Yoon et al., 2015, 2020). Notably, a subsequent buffer washing step caused a transient increase in the $\Delta\lambda_{max}$ signal that approached the baseline value corresponding to a complete DOPC SLB, before the signal dropped again and the final $\Delta\lambda_{max}$ shift after washing was around −0.3 nm relative to the baseline.

In marked contrast, the addition of 500 μM GML to a DOPC SLB caused a transient increase in the $\Delta\lambda_{max}$ signal to around +1.2 nm, which lasted for around 50 min and was followed by an abrupt decrease in the measurement response (Fig. 2c). The corresponding $\Delta\lambda_{max}$ shift after the drop was around −0.4 nm relative to the baseline and there was a high degree of noise in the $\Delta\lambda_{max}$ signal during this stage. A subsequent buffer washing step did not affect the magnitude of the $\Delta\lambda_{max}$ shift, which remained around −0.3 nm, but did cause an appreciable decrease in signal noise. Overall, the LSPR measurement response had four stages that can be summarized as follows: (1) a gradual $\Delta\lambda_{max}$ increase that approached a stable value up to around 50 min; (2) a relatively rapid and spontaneous $\Delta\lambda_{max}$ decrease for around 5 min until a $\Delta\lambda_{max}$ value modestly below the baseline was reached; (3) a rather stable $\Delta\lambda_{max}$ shift with a negative value and high signal noise was reached; and (4) the negative $\Delta\lambda_{max}$ shift response maintained a nearly constant value after buffer washing but had lower signal noise.

Stages 1 to 3 can be understood in terms of the basic mechanistic steps involved in the GML-DOPC SLB interaction process, including nucleation of small buds (stage 1) and coalescence of small buds to form larger buds (stage 2) (Yoon et al., 2015, 2020). Previously, these stages were captured by time-lapsed fluorescence microscopy imaging but could not be discerned in QCM-D measurements (Yoon et al., 2015, 2020). Stage 3 corresponds to a state when large bud coalescence had progressed to a sufficient extent that additional growth, if any, had no further appreciable effect on the $\Delta\lambda_{max}$ shift response with respect to the spatial proximity of DOPC and GML molecules near the sensor surface. The high signal noise during this stage was due to the size of the large buds and adsorbate-induced light scattering effects, which caused fluctuations in the optical extinction spectrum that were not observed in earlier stages of the interaction process or after a buffer washing step (Fig. 3a–c).

Accordingly, the buffer washing step removed the large buds so that only remaining SLB regions on the sensor surface contributed to the net $\Delta\lambda_{max}$ response observed in stage 4. The final $\Delta\lambda_{max}$ shift after washing was around −0.4 nm relative to the baseline and further indicates that the SLB adlayer remained nearly intact while there were some voids resulting from the interaction process. In marked contrast, there were no appreciable fluctuations in the optical extinction spectrum during the

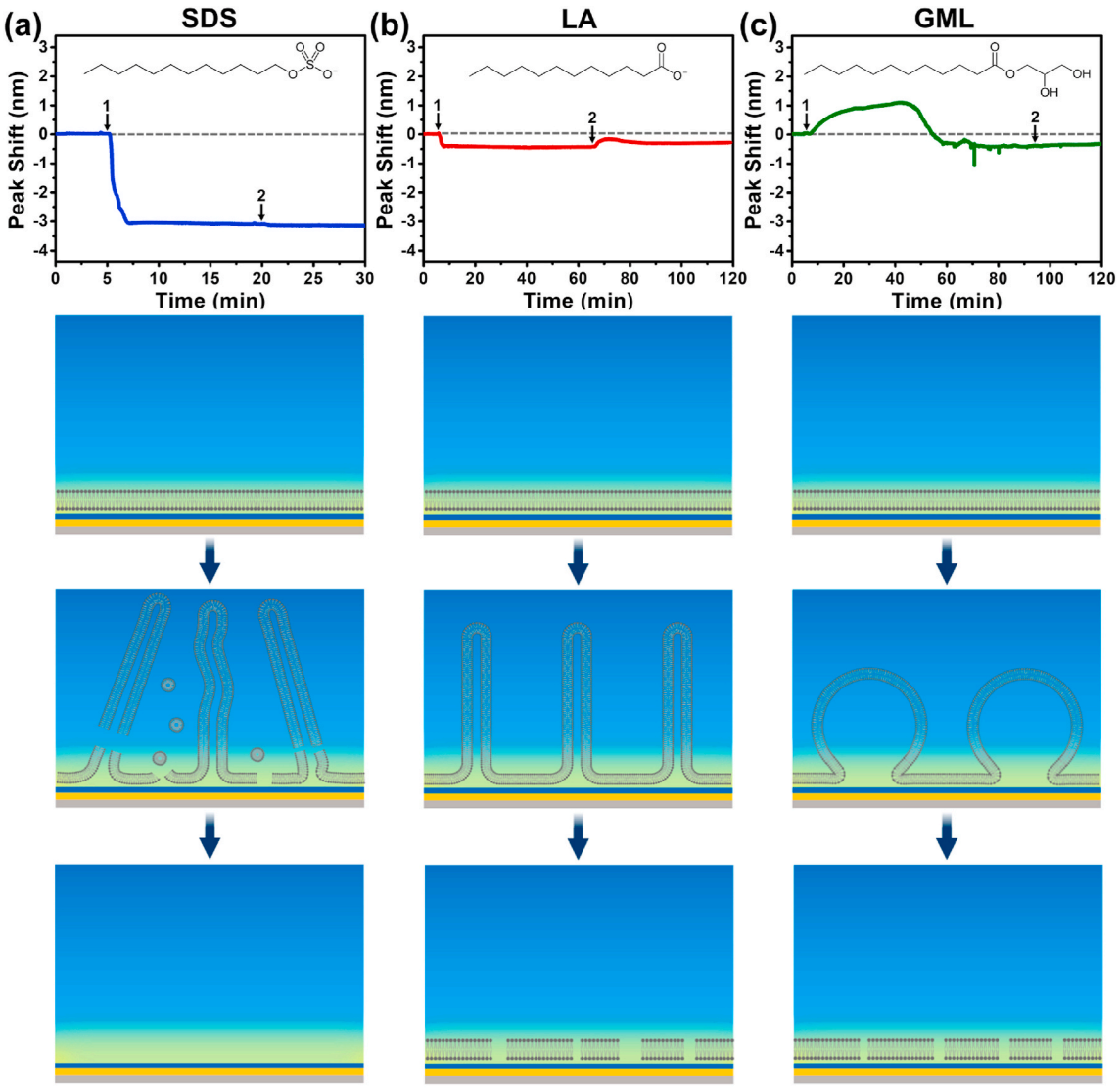

Fig. 2. Real-time LSPR tracking of SDS, LA, and GML interactions with DOPC SLB platforms on silica-coated gold nanodisk arrays. Data correspond to SLB treatment with (a) 2 mM SDS, (b) 2 mM LA, and (c) 500 μM GML. Prior to measurement, a DOPC SLB was fabricated on the sensor surface and the $\Delta\lambda_{max}$ signal was set to zero. Then, an initial baseline of the SLB-coated sensor surface in aqueous buffer solution was recorded before compounds were added to the SLB platform under continuous flow conditions starting at $t = 5$ min (see first arrow labeled "1"). A buffer washing step was performed after the measurement signal stabilized (see second arrow labeled "2"). The molecular structures of SDS, LA, and GML are presented as insets in the respective graphs. Schematic illustrations of the membrane morphological changes corresponding to the SDS, LA, and GML interaction cases are also shown below each graph.

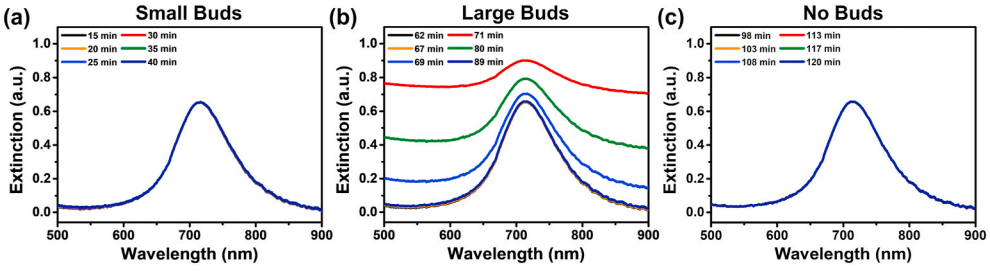

Fig. 3. Time-lapse extinction spectra of DOPC SLB-coated nanodisk array during different stages of the GML-DOPC SLB interaction process. Six representative spectra are presented for (a) small bud growth regime upon GML addition, (b) large bud growth regime due to bud coalescence and before buffer washing, and (c) remaining SLB adlayer after a buffer washing step was performed. Time points correspond to the kinetic data in Fig. 2c. Note that the spectra are superimposed in panels (a) and (c) due to lack of spectral change.

SDS or LA interaction processes, supporting that only large buds but neither small buds nor tubules cause such effects based on the experimental data (Fig. S1).

Fig. 4a summarizes the maximum $\Delta\lambda_{max}$ shifts that occurred during each of these three interaction cases. For the SDS case, there was a sharp, one-step drop in the $\Delta\lambda_{max}$ signal and hence the maximum $\Delta\lambda_{max}$ shift corresponded to a final value around -3.15 ± 0.09 nm. Likewise, for the LA case, the maximum $\Delta\lambda_{max}$ shift was around -0.48 ± 0.03 nm. Thus, the maximum $\Delta\lambda_{max}$ shifts in the SDS and LA cases had negative values below the baseline, indicating that the spatial proximity of adsorbed

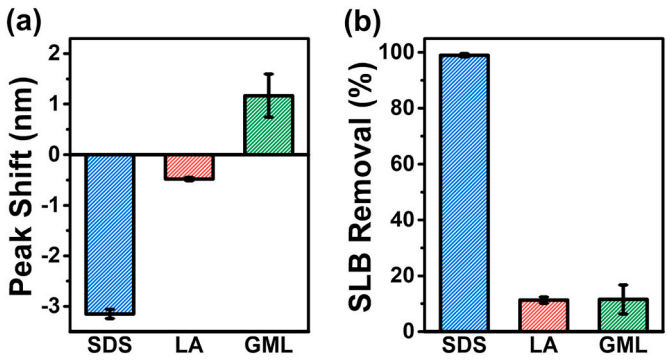

Fig. 4. Quantitative comparison of (a) maximum LSPR measurement response and (b) surface area percentage of SLB removal corresponding to SDS, LA, and GML treatment of DOPC SLBs. Analysis is based on data presented in Fig. 2. Mean ± standard deviation values were calculated from 3 independent experiments per test group.

lipid molecules moved away, on average, from the sensor surface due to solubilization (irreversible) or membrane remodeling (partially reversible). By contrast, the maximum $\Delta\lambda_{max}$ shift in the GML case was around $+1.17 \pm 0.43$ nm, which supports that bud formation caused a distinct measurement response that is likely related to GML attachment during the initial stages of small bud nucleation.

We also quantified the fractional amount of SLB adlayer that was removed due to the interactions with SDS, LA, and GML (Fig. 4b). The SDS interaction caused 98.95 ± 0.62% removal, while LA and GML interactions caused around 11.28 ± 1.11% and 11.52 ± 5.18% removal, respectively. Note that the calculated percentages of SLB removal are lower bound estimates because the antimicrobial compounds (especially LA and GML) might intercalate into the SLB. Based on past experimental results (Yoon et al., 2017) and the known tendency for single-chain lipid amphiphiles to have short residence times in planar membrane configurations, such effects are expected to be modest and the removal percentages obtained by the LSPR measurements agree well with past fluorescence microscopy imaging results (Yoon et al., 2020). SLB removal implies the presence of voids, which likely correspond to regions where three-dimensional tubules or buds protruded from the SLB. During the buffer washing step, tubules and buds became detached when the bulk solution is exchanged from a LA- or GML-containing solution to buffer solution without these species, resulting in the voids. In addition, compared to the DOPC SLB, the LA- and GML-containing tubules and buds represent new phases with spontaneous curvature (Yoon et al., 2020). Accordingly, the intercalation of LA and GML species in the planar SLB is expected to be thermodynamically unfavorable.

Hence, the high surface sensitivity of the LSPR measurement response is able to track complex membrane remodeling processes related to SDS, LA, and GML interactions with SLBs as well as to characterize SLB adlayer properties. Of particular note, the LSPR measurement response demonstrated high sensitivity to tracking different stages of the GML-induced membrane budding process, which were not previously detected in QCM-D measurements in which case hydrodynamic effects – stemming from changes in the amount of hydrodynamically-coupled solvent as opposed to changes in membrane morphology itself – dominated the measurement response and masked the different interaction stages. By contrast, the LSPR measurement readout is directly related to changes in the shape configuration and location of adsorbed biomacromolecules relative to the sensor surface and is not sensitive to hydrodynamically-coupled solvent molecules, which allowed detailed tracking of different stages involved in the complex remodeling process.

3.2. Theoretical analysis of membrane morphological changes

To further analyze the experimental results, we developed a theoretical model to describe how the LSPR measurement response depends on the type of membrane remodeling event and the specific geometrical properties of lipid protrusions that form. In general, the LSPR-enhanced electromagnetic field decay can be described by various models and we use the dipole approximation due to its physical accuracy and mathematical simplicity (Jackman et al., 2014).

In the present experiments, SDS, LA, and GML interact with a DOPC SLB. The SLB thickness, l_s, is much smaller than the length of the LSPR-enhanced electromagnetic field penetration, and accordingly the LSPR $\Delta\lambda_{max}$ shift corresponding to an SLB is proportional to l_s and, in the absence of SDS, LA, and GML, is given by

$$\Delta\lambda_{max} = \Delta\lambda_{max}^{SLB} \equiv Cl_s, \quad (1)$$

where C is a proportionality constant that depends on the size and optical properties of the nanodisks as well as on the optical properties of the SLB. After SDS, LA, or GML attachment, the resulting $\Delta\lambda_{max}$ shift depends on the shape, size, and arrangement of the nano- or microstructures formed as part of the membrane remodeling process that is triggered by these species.

In the SDS case, the attachment is accompanied by transient tubule formation and rapid detachment of the SDS-DOPC-interaction product. The detachment process is the dominant effect manifested in the LSPR measurement response and, after complete removal of DOPC lipids from the sensor surface, SDS does not attach further to the surface. Thus, relative to the baseline signal in aqueous solution before lipid attachment, we have

$$\Delta\lambda_{max} = Cl_s(1-f) \equiv \Delta\lambda_{max}^{SLB}(1-f), \quad (2)$$

where f is the SLB fraction that is removed from the sensor surface. If the baseline signal corresponds to a complete, prefabricated DOPC SLB, then the $\Delta\lambda_{max}$ shift can be obtained by subtracting eq. (1) from eq. (2), *i.e.*,

$$\Delta\lambda_{max} = -\Delta\lambda_{max}^{SLB} f. \quad (3)$$

Eq. (3) describes the negative $\Delta\lambda_{max}$ shift that is depicted in Fig. 2a.

On the other hand, LA and GML attachment to a DOPC SLB is accompanied by the formation of persistent tubules and buds, respectively. As already mentioned above, the appearance of these structures is expected to be related to phase separation in the SLB and spontaneous curvature of the newly formed phase (Yoon et al., 2020) [for buds, this mechanism was proposed in the seminal article by Jülicher and Lipowsky (1993)]. The thickness and optical properties of the lipid bilayer in different phases are slightly different. This factor is, however, minor compared to the SLB restructuring at the nano- or microscale and can be ignored. The key factor is the SLB restructuring itself. We consider that the corresponding structures, tubules or buds, are located at random [this is validated by our past fluorescence microscopy observations (Yoon et al., 2015, 2020)] and operate with their average shape and size (this is a reasonable approximation). The basements of tubules and buds with varying geometries are considered to be free of attached biomacromolecules in all cases (Fig. 5). In principle, with our present knowledge, material attachment there cannot be excluded, but statistically and kinetically this appears to be unlikely. Under such conditions, the LSPR $\Delta\lambda_{max}$ shift, calculated with respect to the λ_{max} signal corresponding to an adsorbate-free sensor surface, can be represented as

$$\Delta\lambda_{max} = Cl_s[(1-f)+\chi f] \equiv \Delta\lambda_{max}^{SLB}[(1-f)+\chi f], \quad (4)$$

where $(1-f)$ is the fraction of the support area that is covered by the SLB [as in eq. (2)], f is the fraction of the support area associated with tubule or bud basements, and $\chi \equiv \delta_2/\delta_1$ is the dimensionless factor that is defined as the ratio of the contribution (to the LSPR signal) of a single tubule or bud to that of an SLB fragment with an area equal to the area of

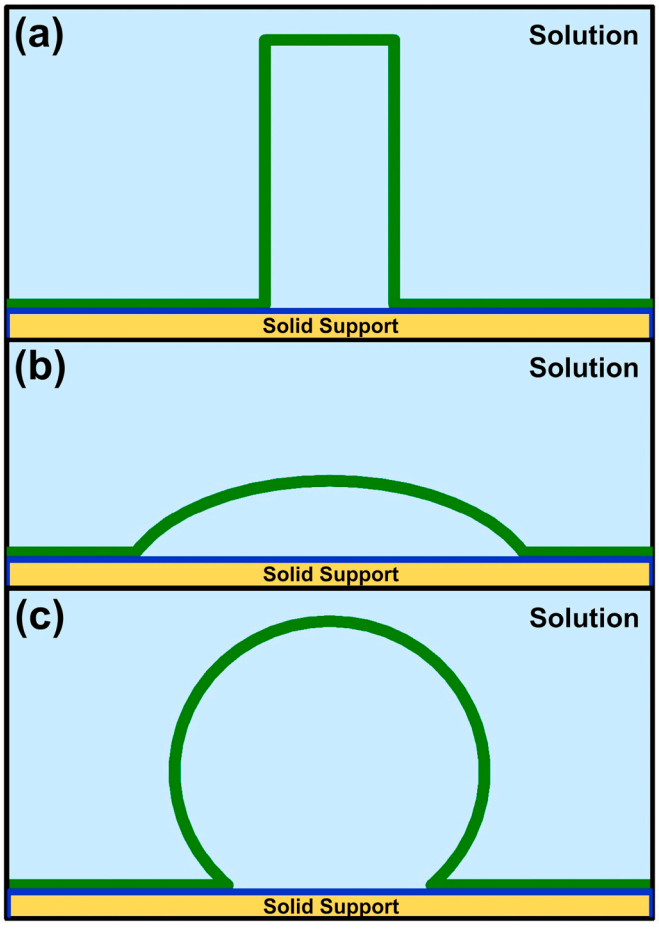

Fig. 5. Schematic illustrations of (a) tubule, (b) cap-like bud, and (c) spherical bud protrusions on a silica-coated sensor surface. Lipid bilayer, silica coating, and gold nanodisk transducer structures are represented by green, blue, and yellow-gold colors, respectively. Note that the basement region for each type of protrusion is devoid of attached biomacromolecules. (For interpretation of the references to color in this figure legend, the reader is referred to the Web version of this article.)

the tubule or bud basement. If the baseline signal corresponds to a complete, prefabricated SLB, then we should subtract eq. (1) from eq. (4), *i.e.*,

$$\Delta\lambda_{\max} = -\Delta\lambda_{\max}^{\mathrm{SLB}}(1-\chi)f. \tag{5}$$

To calculate χ, we consider that tubules are oriented perpendicular to the support (Fig. 5a; the results for other orientations can be obtained by analogy). Buds are represented as truncated spheres (Fig. 5b and c). In both of these cases, the basements are circular, and we have

$$\delta_1 \sim \pi r^2, \tag{6}$$

where r is the corresponding radius. The contribution of a tubule or bud to the LSPR signal is proportional to the convolution of the tubule or bud area with a factor taking the extinction of the LSPR-enhanced electromagnetic field into account. In the dipole approximation, this factor is proportional to $A/(R_* + z)^6$, where R_* is the effective radius corresponding to the regions making the main contribution to the LSPR signal, and A is a constant that can be chosen depending on the context (Ferhan et al., 2018; Jackman et al., 2014, 2017b). In our present context, we use $A = R_*^6$ and accordingly represent δ_2 as

$$\delta_2 \sim \int_0^h \frac{ds}{dz}\frac{R_*^6}{(R_* + z)^6}dz, \tag{7}$$

where h is the tubule or bud height, and ds/dz is the derivative defined as the ratio of an element of the tubule or bud area (located between z and $z + dz$) to dz. To explain the choice of this expression for A, we note that for objects with small height ($h \ll R_*$), we can neglect z in $(R_* + z)^6$, and accordingly

$$\delta_2 \sim \int_0^h ds = s. \tag{8}$$

For a disk-like object, we have $s = \pi r^2$, where r is the object radius, and accordingly the right-hand side of expression (7) for δ_2 is identical in this limit to the right-hand side of expression (6) for δ_1. Thus, we can directly compare expressions (6) and (7). In particular, we obtain

$$\chi = \frac{\delta_2}{\delta_1} = \int_0^h \frac{ds}{dz}\frac{R_*^6}{\pi r^2(R_* + z)^6}dz. \tag{9}$$

For tubules oriented perpendicularly to the support, we have $ds/dz = 2\pi r$. With this specification, eq. (9) yields

$$\chi = \frac{2R_*}{5r}\left(1 - \frac{R_*^5}{(R_* + h)^5}\right). \tag{10}$$

If the tubule length is short, $h < R_*$, we obtain $R_*^5/(R_* + h)^5 \cong 1 - 5h/R_*$, and accordingly

$$\chi \cong 2h/r. \tag{11}$$

As it should be in this limit, this is just the ratio of the tubule area $2\pi rh$ to the basement area, πr^2. In another limit when the tubules are long, $h \gg R_*$, we have $R_*^5/(R_* + h)^5 \ll 1$, and accordingly this ratio can be neglected in eq. (10), *i.e.*,

$$\chi \cong 2R_*/5r. \tag{12}$$

In our case, the length of tubules is short only during the very beginning of their growth. Neglecting this stage, we can incorporate expression (12) into eq. (5), *i.e.*,

$$\Delta\lambda_{\max} = -\Delta\lambda_{\max}^{\mathrm{SLB}}(1 - 2R_*/5r)f. \tag{13}$$

In our experiments with LA (cf. Fig. 2b), tubule formation occurred rapidly in the beginning and the corresponding $\Delta\lambda_{\max}$ shift was negative and relatively small (compared to $\Delta\lambda_{\max}^{\mathrm{SLB}}$) but not very small. f was also relatively small. In terms of expression (13), this means that $(1 - 2R_*/5r)$ should be positive and not too close to zero, *i.e.*, we should have $R_*/r < 1$. Practically, this roughly means that the tubule diameter should be comparable with or larger than the gold nanodisk diameter.

Alternatively, if a bud with height h and basement radius r is represented by a truncated sphere (cf. Fig. 5b and c), then the radius of its curvature is $\rho = (r^2 + h^2)/2h$, and $ds/dz = 2\pi\rho \equiv \pi(r^2 + h^2)/h$ [the fact that, in this case, ds/dz is independent of z was earlier used in the contexts of TIRF (Olsson et al., 2015), SPR (Rupert et al., 2016), and LSPR (Ferhan et al., 2018) measurements]. With this specification, eq. (9) yields

$$\chi = \frac{(r^2 + h^2)R_*}{5hr^2}\left(1 - \frac{R_*^5}{(R_* + h)^5}\right). \tag{14}$$

Then, by analogy with eqs. 10–13, one can obtain the following expressions for small and large buds

$$\chi \cong \left(r^2 + h^2\right)/r^2 \text{ for } h < R_*, \tag{15}$$

$$\chi = \frac{\left(r^2 + h^2\right)R_*}{5hr^2} \text{ for } h \gg R_*, \tag{16}$$

and accordingly, the respective LSPR measurement responses can be described by

$$\Delta\lambda_{\max} = -\Delta\lambda_{\max}^{\mathrm{SLB}}\left[1 - \left(r^2 + h^2\right)/r^2\right]f \text{ for } h < R_*, \tag{17}$$

$$\Delta\lambda_{\max} = -\Delta\lambda_{\max}^{\mathrm{SLB}}\left[1 - \frac{\left(r^2 + h^2\right)R_*}{5hr^2}\right]f \text{ for } h \gg R_*. \tag{18}$$

In our experiments with GML (cf. Fig. 2c), the $\Delta\lambda_{\max}$ shift was positive and appreciable up to about 50 min. During this stage, there is primarily formation of numerous small nuclei of buds so that their height is somewhat larger than that of the basement radius. This case is expected to be described by using eq. (17). With $f \cong 0.3$, the observed measurement response can be explained by assuming $r \cong h < R_*$. This assumption appears to be physically reasonable. Afterwards, the nuclei rapidly coalesce and form large buds. During this stage, the $\Delta\lambda_{\max}$ shift was negative and appreciable. It can be described by employing eq. (18). Using again $f \cong 0.3$, we conclude that the ratio $(r^2 + h^2)R_*/(5hr^2)$ should be small ($\ll 1$). Practically, this means that we should have $R_*/r \ll 1$. This conclusion is confirmed by our past fluorescence microscopy observations (Yoon et al., 2020) and the transition in the $\Delta\lambda_{\max}$ shift response from small buds to large buds is further supported by the experimentally observed fluctuations in the optical extinction spectrum that occurred for large, but not small, buds (cf. Fig. 3).

The theoretical formalism developed above is based on the LSPR-related dipole approximation. In principle, one can alternatively use the exponential approximation (Larsson et al., 2009), which physically corresponds to the sensing concepts underpinning the SPR or TIRF microscopy techniques. To extend the applicability of the theoretical part of our work, we have additionally reworded our theoretical results in terms of the exponential approximation (see Supplementary Information for more details) so that they can be directly used in the SPR or TIRF microscopy contexts for relevant biosensing applications.

4. Conclusions

In this study, we have shown that real-time LSPR measurements can distinguish and track distinct types of three-dimensional membrane morphological changes in an SLB adsorbate based on the corresponding measurement signatures provided the scale of sizes of the corresponding structures is known. While it has been recently shown that LSPR measurements can detect subtle conformational changes in adsorbed biomacromolecules that can be treated analytically as uniform films or spherically shaped structures, our findings demonstrate a new angle of biosensing capabilities to detect large-scale, non-uniform shape changes in adsorbed biomacromolecules. The sensing concept was validated in experiments involving three-dimensional membrane morphological changes triggered by antimicrobial fatty acids, monoglycerides, and surfactants in micellar form. Aside from detecting the distinct morphological changes occurring in each case, our findings also establish a theoretical framework to understand how the growth and evolution of different types of adsorbate protrusions yield complex, multi-step measurement signatures that can be used to classify the membrane-disruptive properties of different antimicrobial compounds and other membrane-active compounds. Importantly, such capabilities demonstrate superior advantages to biosensing techniques used in past works and the nanoplasmonic sensing approach is also compatible with a wide range of biomimetic lipid compositions to enable numerous sensing and diagnostic application opportunities.

CRediT authorship contribution statement

Bo Kyeong Yoon: Conceptualization, Investigation, Writing - original draft, Writing - review & editing. **Hyeonjin Park:** Investigation, Writing - review & editing. **Vladimir P. Zhdanov:** Conceptualization, Methodology, Writing - original draft, Writing - review & editing. **Joshua A. Jackman:** Conceptualization, Writing - original draft, Writing - review & editing, Supervision. **Nam-Joon Cho:** Conceptualization, Writing - review & editing, Supervision.

Declaration of competing interest

The authors declare that they have no known competing financial interests or personal relationships that could have appeared to influence the work reported in this paper.

Acknowledgements

This work was supported by the National Research Foundation of Korea (NRF) grant funded by the Korean government (MSIT) (No. 2020R1C1C1004385), and by the Korea Research Fellowship Program through the National Research Foundation of Korea (NRF) funded by the Ministry of Science and ICT (2019H1D3A1A01070318). Schematic illustrations were created with BioRender.com under an academic lab subscription.

Appendix A. Supplementary data

Supplementary data to this article can be found online at https://doi.org/10.1016/j.bios.2020.112768.

References

Agnarsson, B., Wayment-Steele, H., Höök, F., Kunze, A., 2016. Nanoscale 8 (46), 19219–19223.
Bruzas, I., Unser, S., Yazdi, S., Ringe, E., Sagle, L., 2016. Anal. Chem. 88 (16), 7968–7974.
Buck, J., Grossen, P., Cullis, P.R., Huwyler, J., Witzigmann, D., 2019. ACS Nano 13 (4), 3754–3782.
Cho, N.-J., Dvory-Sobol, H., Lee, C., Cho, S.-J., Bryson, P., Masek, M., Elazar, M., Frank, C.W., Glenn, J.S., 2010. Sci. Transl. Med. 2 (15), 15ra16.
Cho, N.-J., Pham, E.A., Hagey, R.J., Leveque, V.J., Ma, H., Klumpp, K., Glenn, J.S., 2016. ACS Cent. Sci. 2 (7), 456–466.
Dahlin, A.B., Tegenfeldt, J.O., Höök, F., 2006. Anal. Chem. 78 (13), 4416–4423.
Dahlin, A.B., Wittenberg, N.J., Höök, F., Oh, S.-H., 2013. Nanophotonics 2 (2), 83–101.
Di Iorio, D., Lu, Y., Meulman, J., Huskens, J., 2020. Chem. Sci. 11 (12), 3307–3315.
Ferhan, A.R., Špačková, B., Jackman, J.A., Ma, G.J., Sut, T.N., Homola, J., Cho, N.-J., 2018. Anal. Chem. 90 (21), 12503–12511.
Han, W.B., Kang, D.-H., Na, J.-H., Yu, Y.G., Kim, T.S., 2019. Biosens. Bioelectron 141, 111404.
Jackman, J.A., Cho, N.-J., 2020. Langmuir 36 (6), 1387–1400.
Jackman, J.A., Zhdanov, V.P., Cho, N.-J., 2014. Langmuir 30 (31), 9494–9503.
Jackman, J.A., Špačková, B., Linardy, E., Kim, M.C., Yoon, B.K., Homola, J., Cho, N.-J., 2016. Chem. Commun. 52 (1), 76–79.
Jackman, J.A., Ferhan, A.R., Cho, N.-J., 2017a. Chem. Soc. Rev. 46 (12), 3615–3660.
Jackman, J.A., Ferhan, A.R., Yoon, B.K., Park, J.H., Zhdanov, V.P., Cho, N.-J., 2017b. Anal. Chem. 89 (23), 12976–12983.
Jackman, J.A., Yorulmaz Avsar, S., Ferhan, A.R., Li, D., Park, J.H., Zhdanov, V.P., Cho, N.-J., 2017c. Anal. Chem. 89 (2), 1102–1109.
Jose, J., Jordan, L.R., Johnson, T.W., Lee, S.H., Wittenberg, N.J., Oh, S.H., 2013. Adv. Funct. Mater. 23 (22), 2812–2820.
Jülicher, F., Lipowsky, R., 1993. Phys. Rev. Lett. 70 (19), 2964–2967.
Kolahdouzan, K., Jackman, J.A., Yoon, B.K., Kim, M.C., Johal, M.S., Cho, N.-J., 2017. Langmuir 33 (20), 5052–5064.
Langhammer, C., Larsson, E.M., Kasemo, B., Zoric, I., 2010. Nano Lett. 10 (9), 3529–3538.
Larsson, E.M., Edvardsson, M.E.M., Langhammer, C., Zoric, I., Kasemo, B., 2009. Rev. Sci. Instrum. 80, 125105.
Lee, H.R., Lee, Y., Oh, S.S., Choi, S.Q., 2020. Small. https://doi.org/10.1002/smll.202002541.
Mapar, M., Joemetsa, S., Pace, H., Zhdanov, V.P., Agnarsson, B., Höök, F., 2018. J. Phys. Chem. Lett. 9 (17), 5143–5149.
Nishio, M., Teranishi, Y., Morioka, K., Yanagida, A., Shoji, A., 2020. Biosens. Bioelectron 150, 111918.
Oh, S.-H., Altug, H., 2018. Nat. Commun. 9, 5263.
Olsson, T., Zhdanov, V.P., Höök, F., 2015. J. Appl. Phys. 118 (6), 064702.

Park, Y., Kang, B., Ahn, C.H., Cho, H.K., Kwon, H., Park, S., Kwon, J., Choi, M., Lee, C., Kim, K., 2019. Biosens. Bioelectron 142, 111512.
Rahimi, M., Regan, D., Arroyo, M., Subramaniam, A.B., Stone, H.A., Staykova, M., 2016. Biophys. J. 111 (12), 2651–2657.
Rupert, D.L., Shelke, G.V., Emilsson, G., Claudio, V., Block, S., Lässer, C., Dahlin, A., Lötvall, J.O., Bally, M., Zhdanov, V.P., Höök, F., 2016. Anal. Chem. 88 (20), 9980–9988.
Ryu, Y.-S., Yun, H., Chung, T., Suh, J.-H., Kim, S., Lee, K., Wittenberg, N.J., Oh, S.-H., Lee, B., Lee, S.-D., 2019. Biosens. Bioelectron 142, 111568.
Soler, M., Li, X., John-Herpin, A., Schmidt, J., Coukos, G., Altug, H., 2018. ACS Sens. 3 (11), 2286–2295.
Špačková, B., Wrobel, P., Bocková, M., Homola, J., 2016. Proc. IEEE 104 (12), 2380–2408.
Sut, T.N., Jackman, J.A., Yoon, B.K., Park, S., Kolahdouzan, K., Ma, G.J., Zhdanov, V.P., Cho, N.-J., 2019. Langmuir 35 (32), 10658–10666.
Unser, S., Bruzas, I., He, J., Sagle, L., 2015. Sensors 15 (7), 15684–15716.
Varsano, N., Fargion, I., Wolf, S.G., Leiserowitz, L., Addadi, L., 2015. J. Am. Chem. Soc. 137 (4), 1601–1607.
Yoon, B.K., Jackman, J.A., Kim, M.C., Cho, N.-J., 2015. Langmuir 31 (37), 10223–10232.
Yoon, B.K., Jackman, J.A., Kim, M.C., Sut, T.N., Cho, N.-J., 2017. Langmuir 33 (11), 2750–2759.
Yoon, B.K., Jackman, J.A., Valle-González, E.R., Cho, N.-J., 2018. Int. J. Mol. Sci. 19 (4), 1114.
Yoon, B.K., Park, S., Ma, G.J., Kolahdouzan, K., Zhdanov, V.P., Jackman, J.A., Cho, N.-J., 2020. J. Phys. Chem. Lett. 11, 4951–4957.